Orbital selective spin waves in detwinned NaFeAs

David W. Tam [1], Zhiping Yin,[2,*] Yaofeng Xie [1], Weiyi Wang,[1] M. B. Stone [3], D. T. Adroja,[4,5] H. C. Walker [4],
Ming Yi,[1] and Pengcheng Dai [1,†]

[1]*Department of Physics and Astronomy, Rice University, Houston, Texas 77005, USA*
[2]*Center for Advanced Quantum Studies and Department of Physics, Beijing Normal University, Beijing 100875, China*
[3]*Quantum Condensed Matter Division, Oak Ridge National Laboratory, Oak Ridge, Tennessee 37831, USA*
[4]*ISIS Facility, Rutherford Appleton Laboratory, STFC, Chilton, Didcot OX11 0QX, United Kingdom*
[5]*Highly Correlated Matter Research Group, Physics Department, University of Johannesburg, P.O. Box 524,
Auckland Park 2006, South Africa*

The existence of orbital-dependent electronic correlations has been recognized as an essential ingredient to describe the physics of iron-based superconductors. NaFeAs, a parent compound of iron-based superconductors, exhibits a tetragonal-to-orthorhombic lattice distortion below $T_s \approx 60$ K, forming an electronic nematic phase with two $90°$ rotated (twinned) domains, and orders antiferromagnetically below $T_N \approx 42$ K. We use inelastic neutron scattering to study spin waves in uniaxial pressure-detwinned NaFeAs. By comparing the data with combined density functional theory and dynamical mean-field theory calculations, we conclude that spin waves up to an energy scale of $E_{crossover} \approx 100$ meV are dominated by d_{yz}-d_{yz} intraorbital scattering processes, which have the twofold (C_2) rotational symmetry of the underlying lattice. On the other hand, the spin wave excitations above $E_{crossover}$, which have approximately fourfold (C_4) rotational symmetry, arise from the d_{xy}-d_{xy} intraorbital scattering that controls the overall magnetic bandwidth in this material. In addition, we find that the low-energy ($E \approx 6$ meV) spin excitations change from approximate C_4 to C_2 rotational symmetry below a temperature T^* ($>T_s$), while spin excitations at energies above $E_{crossover}$ have approximate C_4 rotational symmetry and are weakly temperature dependent. These results are consistent with angle-resolved photoemission spectroscopy measurements, where the presence of a uniaxial strain necessary to detwin NaFeAs also raises the onset temperature T^* of observable orbital-dependent band splitting to above T_s, thus supporting the notion of orbital selective spin waves in the nematic phase of iron-based superconductors.

I. INTRODUCTION

High-temperature superconductivity in the copper oxides and iron pnictides arises from electron and hole doping of their respective antiferromagnetically ordered parent compounds [1,2]. In the case of copper oxide superconductors, the parent compounds are Mott insulators with strong electron correlations [3], and superconductivity arises from electron pairing in the CuO_2 plane from the one-electron $d_{x^2-y^2}$ Cu orbitals [4]. For iron pnictide superconductors, the parent compounds such as $BaFe_2As_2$ and NaFeAs are semimetallic [5], and antiferromagnetism can be generated either by Fermi surface nesting of itinerant electrons [6] or local moments mediated by superexchange interactions through the As anions [Fig. 1(a)] [7]. Instead of the single $d_{x^2-y^2}$ band in copper oxides, the electronic structure of iron pnictides near the Fermi level contains several active bands with appreciable mixing of the Fe 3d t_{2g} orbitals (d_{xz}, d_{yz}, and d_{xy}) [Figs. 1(b)–1(d)] [8]. Therefore, a fundamental difference between copper oxides and iron pnictides is the multiorbital multiband nature of the underlying electronic structure in iron-based superconductors.

In addition to having collinear antiferromagnetic (AF) order below T_N as shown in Fig. 1(a), iron pnictides exhibit a tetragonal (C_4 symmetric) to orthorhombic (C_2 symmetric) lattice distortion at temperature below T_s ($T_s \gtrsim T_N$) [5], forming an electronic nematic phase with two $90°$ rotated (twinned) domains [Figs. 1(e)–1(h)] [9,10]. In the paramagnetic tetragonal (C_4) and nematic orthorhombic (C_2) phases, the Fermi surfaces of NaFeAs observed by angle-resolved photoemission spectroscopy (ARPES) experiments are schematically shown in Figs. 2(a) and 2(b), respectively [8]. The appearance of a nematic phase is associated with an energy splitting between d_{xz} and d_{yz} orbitals, where the d_{yz} band of the electron Fermi surface at X goes up in energy, while the d_{xz} band at Y goes down in energy [Fig. 2(c)] [8]. The splitting leads to more favorable Fermi surface nesting conditions for the d_{yz} orbital along the AF-ordering direction [Figs. 1(e) and 2(b)], and lowers the rotational symmetry of electronic interactions that give rise to anisotropic spin fluctuations [11]; conversely, spin fluctuations with lower rotational symmetry may themselves generate rotational anisotropy in the orbital channel [12]. The situation is not necessarily the same for strongly coupled, localized electrons, through which spin fluctuations are generated by superexchange interactions taking place between Fe ions across the anion (pnictogen/chalcogen) site, reminiscent of strongly coupled
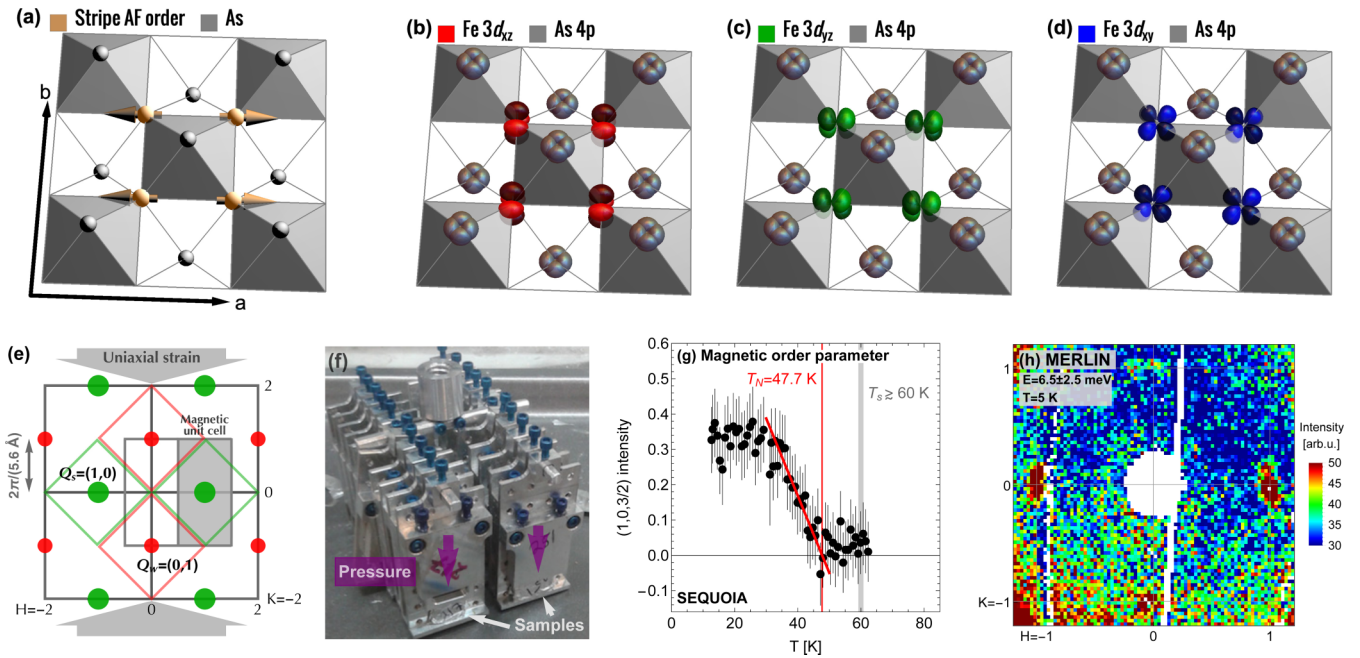
*yinzhiping@bnu.edu.cn
†pdai@rice.edu

FIG. 1. (a) Real-space spin structure of stripe-antiferromagnetically ordered NaFeAs. (b)–(d) Fe $3d$ orbital wave functions projected into the real-space configuration, shown for d_{xz} in red, d_{yz} in green, and d_{xy} in blue, corresponding to the color scheme used throughout this work. The As $4p_x$ and $4p_y$ orbitals are shown in gray at each As site. (e) In-plane **Q**-space configuration in a detwinned sample with uniaxial compression along the vertical direction and the corresponding two-iron magnetic unit cell shaded in gray. Magnetic Bragg reflections at $\mathbf{Q}_{AF,strong} = (1, 0)$ and equivalent are shown with green dots, corresponding to favorable nesting conditions for low-energy d_{yz}-d_{yz} intraorbital scattering processes. Broken tetragonal symmetry below T_s removes the equivalent nesting conditions for d_{xz}-d_{xz} processes, with the positions of residual magnetic Bragg peaks from the unfavored domains shown at $\mathbf{Q}_{AF,weak} = (0, 1)$ and equivalent positions shown as smaller red dots. The diamond-shaped zones around each peak show the area of integrated intensity in Fig. 6. (f) A picture of the 20 coaligned NaFeAs crystals in uniaxial pressure devices used in the SEQUOIA and MERLIN experiments. The arrows mark the applied uniaxial pressure direction. (g) Temperature dependence of the elastic scattering at the strong-domain magnetic Bragg peak position $\mathbf{Q} = (1, 0, 1.5)$. (h) A 2D image of $E = 6.5 \pm 2.5$ meV spin waves of NaFeAs at 10 K obtained on MERLIN with incident neutron energy of $E_i = 40$ meV along the c axis.

electrons in the cuprate materials [7]. In the iron-based superconductors, the d_{xy} orbital is most closely positioned to the anions, and it is also the most strongly localized [8]. For example, in FeTe$_{1-x}$Se$_x$ superconductors with a nematic phase but without static AF order [13–15], signatures of the d_{xy} orbital completely vanish from ARPES measurements at high temperature, indicating that the d_{xy} orbital is becoming more localized, possibly entering into an orbital selective Mott phase [7,16] or a highly incoherent state through the formation of large on-site fluctuating moments due to the Hund's rule coupling [17,18]. From scanning tunneling experiments on FeSe, superconductivity is believed to occur via orbital selective Cooper pairing from the d_{yz} orbital submanifold [19].

In the case of NaFeAs, ARPES studies have found that the d_{xy}-dominated band is more strongly renormalized than the same band in other pnictides, but less so than chalcogenides. Thus, one has a system with moderate overall correlation strength [8,9] that may exhibit spin fluctuations from two distinct mechanisms with different intraorbital scattering processes of different correlation strength. Differentiation of these mechanisms has important consequences for the origins of superconductivity [20]. Inelastic neutron scattering experiments on detwinned FeSe [21], underdoped superconducting NaFe$_{0.985}$Co$_{0.015}$As [22], and Ba(Fe$_{1-x}$Co$_x$)$_2$As$_2$ [23] suggest that the neutron spin resonance, a collective magnetic excita-

tion coupled to the superconducting order parameter [24–29], likely arises from orbital selective electron-hole Fermi surface nesting of quasiparticles within the single d_{yz} orbital submanifold.

In previous inelastic neutron scattering work on twinned NaFeAs [30] and AFe$_2$As$_2$ ($A =$ Ca, Ba, Sr) [31–33], it was found that spin waves in NaFeAs have a zone boundary energy lower than that of AFe$_2$As$_2$. These results have been interpreted as due to increased electron-electron correlations from larger pnictogen height [9], consistent with a combined density functional theory (DFT) and dynamical mean-field theory (DMFT) calculation [30,34]. As these results are obtained on twinned samples that obey the C_4 rotational symmetry, one cannot deduce the relationship between spin excitations and orbital degrees of freedom from symmetry considerations alone in the twinned case. Although recent spin wave measurements on detwinned BaFe$_2$As$_2$ reveal strong magnetic anisotropy between the AF wave vector $\mathbf{Q}_{strong} = (1, 0)$ and $\mathbf{Q}_{weak} = (0, 1)$ in the collinear AF state below the ordering temperature T_N [35], the nearly coupled structural and AF phase transitions in BaFe$_2$As$_2$ [36,37] prevent a determination of the relationship between the $\mathbf{Q}_{strong} = (1, 0)$ and $\mathbf{Q}_{weak} = (0, 1)$ magnetic anisotropy and nematic (structural) phase transition below T_s. On the other hand, NaFeAs exhibits a tetragonal-to-orthorhombic structural transition at $T_s \approx 60$ K
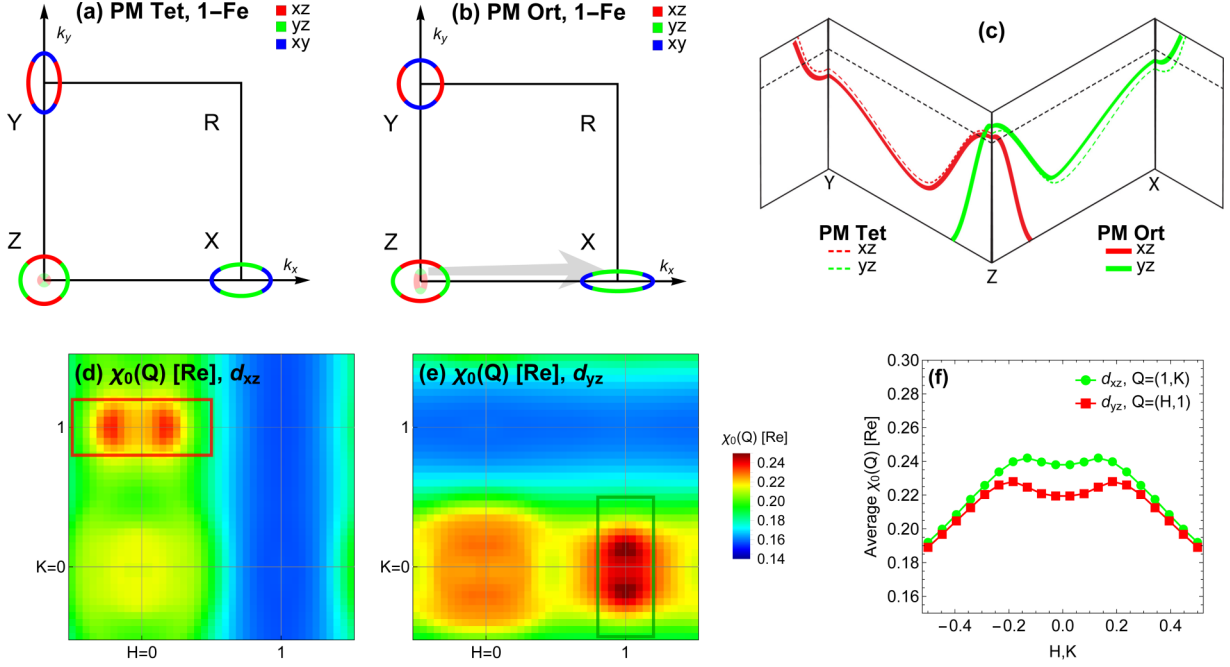
FIG. 2. (a) Fermi surface nesting scheme in the high-temperature paramagnetic tetragonal phase and (b) detwinned paramagnetic orthorhombic phase stable for T_N (≈ 45 K) $< T < T_s$ (≈ 60 K). The gray arrow in (b) shows the position of favorable nesting for d_{yz}-d_{yz} intraorbital scattering at $\mathbf{Q}_{AF,strong} = (1, 0, 1)$ between the inner hole-like pocket at $Z = (0, 0, 1)$ and the elongated electron pocket at $X = (1, 0, 0)$. ARPES data indicate that the inner hole pocket is strictly closed at $Z = (0, 0, 1)$ in the high-temperature phase, and just touches the Fermi level in the paramagnetic orthorhombic phase. Therefore, we show this pocket in light shading to reflect the fact that nesting at $\mathbf{Q}_{AF,strong} = (1, 0, 1)$ may still be satisfied for very low energy scattering processes or for a slightly different choice of k_z values, for example from $(0,0,0.9)$ to $(1, 0, -0.1)$. To further clarify details about the three-dimensionality of the nesting condition, we show the full 3D case in the Supplementary Material [42]. (c) The effect of tetragonal-orthorhombic structure on the d_{xz} and d_{yz} orbital electronic structures of NaFeAs [49,50]. (d), (e) The calculated wave-vector dependence of the real part of the bare susceptibility, $\chi_0(E, \mathbf{Q})[\text{Re}]$, for (d) d_{xz} and (e) d_{yz} orbitals at zero energy ($E = 0$). (f) The intensity of $\chi_0(E, \mathbf{Q})[\text{Re}]$ for d_{xz} and d_{yz} orbitals at $(0,1)$ and $(1,0)$ positions, respectively.

and a separate collinear AF order below $T_N \approx 42$ K at $\mathbf{Q}_{AF} = (1, 0)$ [Fig. 1(g)] [38,39]. Thus, detwinned NaFeAs not only presents a platform for testing the relationship between itinerant and localized physics in different orbital degrees of freedom, but also tests how spin waves are associated with the nematic phase across T_s.

II. EXPERIMENTAL DETAILS

Our inelastic neutron scattering experiments are carried out at the SEQUOIA [40] and MERLIN [41] neutron time-of-flight chopper spectrometers, located, respectively, at the Spallation Neutron Source, Oak Ridge National Laboratory, and ISIS facility, Rutherford-Appleton Laboratory. We define the wave vector $\mathbf{Q}$ in three-dimensional reciprocal space in Å^{-1} as $\mathbf{Q} = H\mathbf{a}^* + K\mathbf{b}^* + L\mathbf{c}^*$, where H, K, and L are Miller indices and $\mathbf{a}^* = \hat{\mathbf{a}}2\pi/a$, $\mathbf{b}^* = \hat{\mathbf{b}}2\pi/b$, $\mathbf{c}^* = \hat{\mathbf{c}}2\pi/c$ are reciprocal lattice units of the orthorhombic unit cell, where $a \approx 5.6$ Å, $b \approx 5.6$ Å, and $c \approx 7.0$ Å [38,39,42]. Figures 1(a) and 1(e) show schematic diagrams of the collinear AF order in NaFeAs in real and reciprocal space, respectively. In the unstrained state, NaFeAs forms twin structural domains below T_s [Fig. 1(e)]. To overcome this, uniaxial mechanical pressure has been used to favor one twin orientation [43–47]. Twenty single crystals of NaFeAs were aligned and cut into rectangular shapes along the a/b direction, individually potted in hydrogen-free Cytop M glue, and wrapped in aluminum foil

to protect them from exposure to air [Fig. 1(f)]. Since the NaFeAs single crystals are detwinned via uniaxial pressure along the b axis [the vertical arrow direction using aluminum springs in an aluminum manifold as shown in Fig. 1(f)], the AF order occurs at the in-plane wave vector $\mathbf{Q}_{strong} = (\pm 1, 0)$ positions, and there should be no magnetic scattering at $\mathbf{Q}_{weak} = (0, \pm 1)$ positions. For a 100% detwinned sample, the magnetic Bragg peak intensity at the AF in-plane wave vector $\mathbf{Q}_{strong}$ should be a factor of 2 of that at zero pressure, while there should be no observable magnetic Bragg scattering at the $\mathbf{Q}_{weak}$ position [Fig. 1(e)]. In typical neutron triple-axis experiments on one single-crystal sample of iron pnictides, the detwinning ratio of the system can be accurately determined by either comparing the uniaxial pressured induced magnetic Bragg peak intensity gain at $(\pm 1, 0, L)$ or comparing the magnetic Bragg peak intensities at $(\pm 1, 0, L)$ and $(0, \pm 1, L)$ positions, where $L = 1, 3, \ldots$ for BaFe$_2$As$_2$ and $0.5, 1.5, \ldots$ for NaFeAs [43–46]. Unfortunately, the rectangular assembly of 20 single crystals of NaFeAs under uniaxial pressure shown in Fig. 1(f) could not be arranged in the sample environment of a triple-axis experiment. For our measurements using neutron time-of-flight spectrometers with only one sample rotation axis ($A3$, along the b axis), elastic scans at different temperatures were collected by rotating the $A3$ angle of the sample assembly to satisfy the elastic condition ($E = 0$) at the magnetic $(1,0,1.5)$ Bragg reflection and revealed $T_N \approx 47$ K [Fig. 1(g)] [38]. Since it is not possible to rotate the "weak" magnetic

Bragg peak at $(0, \pm 1, 1.5)$ positions onto the detector bank at fixed E_i, one cannot use the above-mentioned method to directly measure the sample assembly detwinning ratio, defined as $\eta = [I(1, 0, 1.5) - I(0, 1, 1.5)]/[I(1, 0, 1.5) + I(0, 1, 1.5)]$, where $I(1, 0, 1.5)$ and $I(0, 1, 1.5)$ correspond to the strong and weak magnetic Bragg peaks, respectively [22]. Nevertheless, one can still determine the sample detwinning ratio η using the low-energy inelastic part of the spin fluctuation spectrum, which at least provides a firm lower bound, and was in fact observed to have one-to-one correspondence to η in previous experiments on the NaFeAs and BaFe$_2$As$_2$ systems [22,23].

We estimate the detwinning ratio η by integrating the inelastic fluctuation spectrum for energies just above the spin anisotropy gap where spin waves appear at both the strong and weak positions. For spin wave energies below 20 meV, the anisotropy is not highly energy dependent, giving us confidence in this method. From the inelastic slice containing $4 \leqslant E \leqslant 9$ meV with $E_i = 40$ meV [Fig. 1(h)], we find that the integrated intensities at the strong (I_s at $\mathbf{Q}_{\text{strong}}$) and weak ($I_w$ at $\mathbf{Q}_{\text{weak}}$) positions can give $\eta = (I_s - I_w)/(I_s + I_w) \approx 50\%$, or a 3:1 domain ratio, only slightly smaller than $\eta \approx 62.4\%$ obtained on one single crystal of NaFe$_{0.985}$Co$_{0.015}$As [22].

Our measurements were carried out with incident neutron energies $E_i = 40, 80, 150,$ and 250 meV at SEQUOIA, and $E_i = 29, 54,$ and 170 meV at MERLIN, with the incident beam always along the c axis. In this experimental geometry, points with a given H, K, and energy transfer are always coupled to specific values of L. A typical constant-energy slice contains data from a wide range of L values spanning at least half of a unit cell along the c-axis direction. We simply average over the L values contained in a given slice, converting the analysis into a two-dimensional (2D) problem. For simplicity, we refer to the (H, K) values without specifying L when the energy and E_i are also specified.

III. EXPERIMENTAL RESULTS

Figures 2(a) and 2(b) schematically illustrate the electron-hole Fermi surfaces of NaFeAs and their nesting conditions above and below T_s for different orbitals [11,48–50]. In the paramagnetic tetragonal state, the electron-hole Fermi surface nesting of the d_{yz}-d_{yz} and d_{xz}-d_{xz} orbital quasiparticles is near the $\mathbf{Q}_{\text{strong}} = (\pm 1, 0)$ and $\mathbf{Q}_{\text{weak}} = (0, \pm 1)$ positions, respectively. When the system is cooled below T_s in the paramagnetic orthorhombic nematic phase, the d_{yz} electron band shifts up in energy while the d_{xz} electron band shifts down [Fig. 2(c)] [49,50]. As a result, the inner hole-like pocket at the zone center that is partially closed along k_z acquires an elliptical shape which improves the nesting condition close to the Fermi level due to the larger d_{yz} spectral weight near $E = 0$, therefore enabling scattering processes involving the d_{yz} orbitals to participate in fluctuations with lower overall energy at approximately $\mathbf{Q}_{\text{strong}} = (\pm 1, 0)$. Similarly, scattering processes with the wave vector close to the $\mathbf{Q}_{\text{weak}}$ direction are more favorable for d_{xz}-d_{xz} orbital hole-electron Fermi surface scattering [51].

To determine quantitatively whether the above Fermi-surface nesting description is appropriate for understanding the collinear AF order in NaFeAs, we calculated the wave vector ($\mathbf{Q}$) dependence of the real part of the bare susceptibility, $\chi_0(E, \mathbf{Q})[\text{Re}]$ [52], at zero energy ($E = 0$) contributed by the Fe d_{xz} and d_{yz} orbitals (intraorbital components). While the Fe d_{xz} orbital component has a peak structure around $\mathbf{Q}_{\text{weak}}$ [Fig. 2(d)], the Fe d_{yz} orbital component peaks around $\mathbf{Q}_{\text{strong}}$ [Fig. 2(e)]. Since the comparison plot in Fig. 2(f) shows a somewhat larger ($\approx 10\%$) bare susceptibility around $(1, 0)$ than that around $(0,1)$, the Fermi surface nesting favors $\mathbf{Q}_{\text{strong}}$ in this compound. However, the Fermi surface nesting itself cannot produce the large anisotropy of the experimental spin excitations between $(1, 0)$ and $(0, 1)$ [Fig. 1(h)]. The two-particle vertex correction strongly enhances this difference and gives rise to the large anisotropy of the spin susceptibility between $(1, 0)$ and $(0, 1)$, defined as $\chi(E, \mathbf{Q}) = \chi_0(E, \mathbf{Q})/[1 - \Gamma \chi_0(E, \mathbf{Q})]$, where Γ is the two-particle vertex function [34]. For example, if $\Gamma \chi_0(E, \mathbf{Q}) = 0.99$ at $(1, 0)$ and $\Gamma \chi_0(E, \mathbf{Q}) = 0.90$ at $(0, 1)$, the spin susceptibility $\chi(E, \mathbf{Q})$ at $(1,0)$ is about 10 times the value at $(0, 1)$. Therefore, both the Fermi surface nesting and the two-particle vertex correction play important roles in forming the AF order at $\mathbf{Q}_{\text{strong}}$.

Figures 3(a)–3(f) show 2D images of spin waves at constant energy transfers of $E = 6.5, 17.5, 50, 65, 85,$ and 120 meV in the AF-ordered state at 10 K. At $E = 6.5 \pm 2.5$ meV, there is clear spin wave anisotropy at the $\mathbf{Q}_{\text{strong}} = (\pm 1, 0)$ and $\mathbf{Q}_{\text{weak}} = (0, \pm 1)$ positions. With increasing energy transfer, spin wave anisotropy between $\mathbf{Q}_{\text{strong}}$ and $\mathbf{Q}_{\text{weak}}$ becomes smaller and spin waves become almost C_4 rotational symmetric around $E = 120 \pm 10$ meV. In addition, spin waves broaden and split in the transverse direction with increasing energy, and merge into the $\mathbf{Q} = (1, 1)$ position where they remain somewhat anisotropic at $E = 120 \pm 10$ meV. Figures 3(g)–3(l), 3(m)–3(r), and 3(s)–3(x) show the corresponding cuts in the d_{xz}-d_{xz}, d_{yz}-d_{yz}, and d_{xy}-d_{xy} intraorbital scattering channels, respectively, from the combined DFT+DMFT calculations. For spin waves from the d_{xz}-d_{xz} orbital quasiparticle excitations [Figs. 3(g)–3(l)], the spectral weight of the spin waves is mostly focused at $\mathbf{Q}_{\text{weak}}$, inconsistent with the observed low-energy spin waves [Figs. 3(a)–3(d)]. On the other hand, spin waves from the d_{yz}-d_{yz} orbital quasiparticle excitations are opposite and have large spectral weight at the $\mathbf{Q}_{\text{strong}}$ positions [Fig. 3(m)–3(r)]. Finally, spin waves from the d_{xy}-d_{xy} orbital scattering have spectral weight at both $\mathbf{Q}_{\text{strong}}$ and $\mathbf{Q}_{\text{weak}}$ with approximate C_4 rotational symmetry [Fig. 3(s)–3(x)].

In previous inelastic neutron scattering work on twinned NaFeAs, low-energy spin excitations are enhanced dramatically below T_s instead of T_N due to spin-lattice coupling [53]. To determine whether spin excitation anisotropy at $\mathbf{Q}_{\text{strong}}$ and $\mathbf{Q}_{\text{weak}}$ in NaFeAs is also controlled by the nematic phase below T_s, we summarize in Fig. 4 the temperature dependence of the spin excitations at different energies across T_N and T_s. Figures 4(a)–4(e) and 4(f)–4(j) plot the temperature evolution of spin waves at $E = 6.5 \pm 2.5$ meV and $E = 55 \pm 5$ meV, respectively. Figures 4(k), 4(l), and 4(m) show the temperature dependence of the spin excitation peak intensity at $\mathbf{Q}_{\text{strong}}$ and $\mathbf{Q}_{\text{weak}}$ for energies $E = 6.5 \pm 2.5$, $E = 45 \pm 5$, and $E = 75 \pm 5$ meV, respectively. Since the widths of spin excitations at these energies are identical for $\mathbf{Q}_{\text{strong}}$ and $\mathbf{Q}_{\text{weak}}$ and only
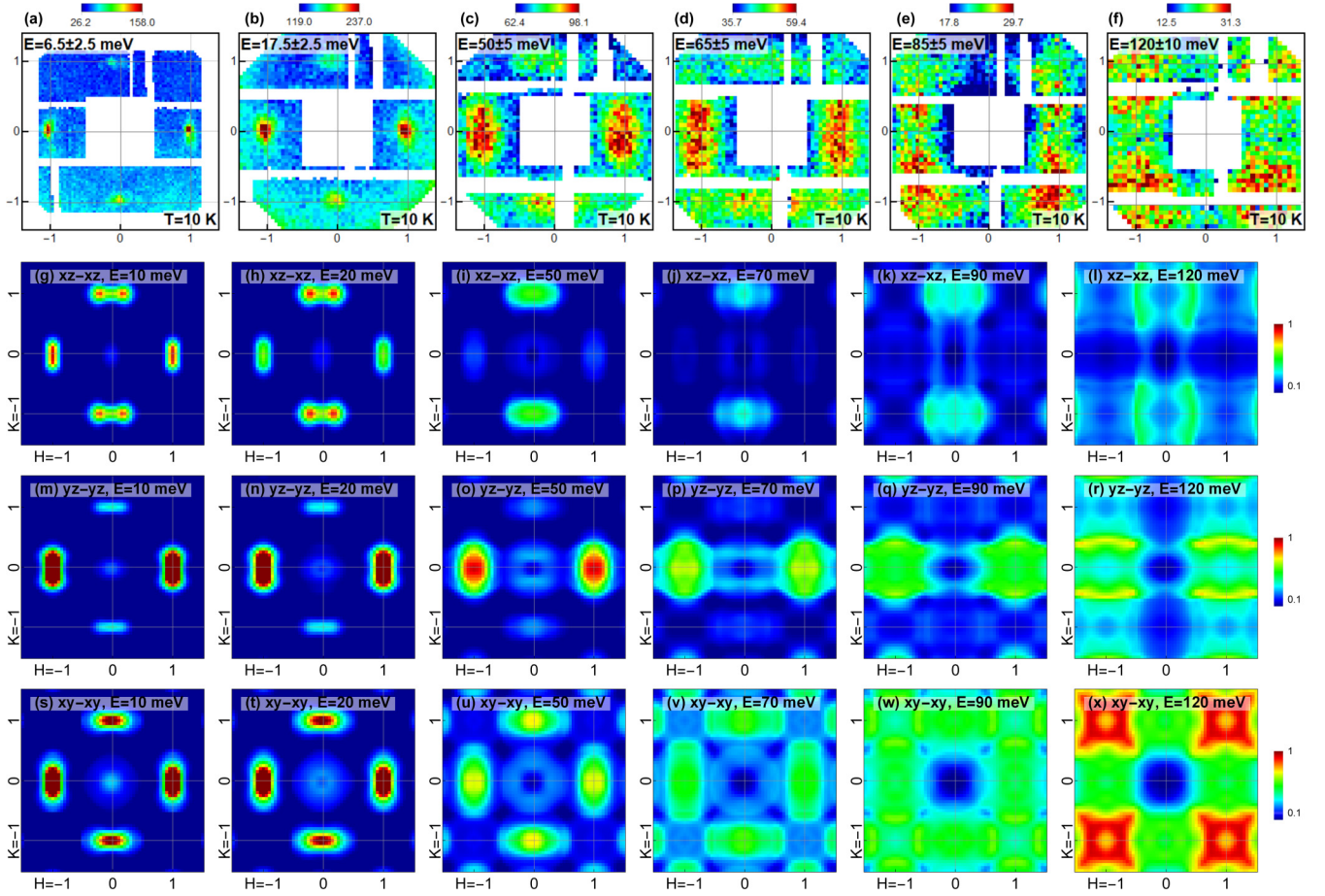
FIG. 3. (a)–(f) Inelastic neutron scattering data from SEQUOIA at $T = 10$ K, for energy transfer $E = 6.5 \pm 2.5$, 17.5 ± 2.5, 50 ± 5, 65 ± 10, 85 ± 5, and 120 ± 10 meV, in absolute units with color scale shown above. Below, corresponding constant-energy slices from the DFT+DMFT calculation, in the d_{xz}-d_{xz} [(g)–(l)], d_{yz}-d_{yz} [(m)–(r)], and d_{xy}-d_{xy} [(s)–(x)] intraorbital scattering channels, for similar energies compared with the neutron scattering data as shown in each panel, and the corresponding intensity scale to the right of each row. The anisotropy of the d_{yz}-d_{yz} channel best resembles the low-energy measurements, but only d_{xy}-d_{xy} processes capture the migration of intensity to the $\mathbf{Q} = (1, 1, L)$ position at high energies. The d_{xz}-d_{xz} channel (second row) exhibits an orientation and anisotropy in the opposite sense from the data. The color scale is fixed for all panels except the top row. The d_{xy} orbital data in (u)–(w) is broader in $\mathbf{Q}$ and has large weakly dispersive background scattering, thus giving a comparable integrated intensity to that of the d_{yz} orbital in the diamond-shaped zones depicted in Fig. 1(e) and Fig. 5(f), despite a smaller peak intensity at (1,0).

weakly temperature dependent as shown in the Supplemental Material [42], the temperature dependence of the peak intensity should give an accurate account of the spin excitation anisotropy.

For spin excitations at $E = 6.5 \pm 2.5$ meV, we find enhanced magnetic scattering at a temperature T^* above T_s marked as a wide dark line, different from that of previous work on unstrained twinned NaFeAs [53]. In addition, a strong magnetic excitation anisotropy between $\mathbf{Q}_{\text{strong}}$ and $\mathbf{Q}_{\text{weak}}$ is also established at temperatures across T_s, and persists to temperatures above T_s [Fig. 4(k)]. Upon increasing excitation energies to $E = 45 \pm 5$ [Fig. 4(l)] and 75 ± 5 [Fig. 4(m)] meV, spin excitation anisotropy is also present to temperatures above T_s. These results are consistent with ARPES and transport measurements on both NaFeAs and Ba(Fe$_{1-x}$Co$_x$)$_2$As$_2$, where anisotropy reflecting the nematic order is observed to begin at a temperature T^* above the zero pressure T_s due to the applied uniaxial pressure necessary to detwin and maintain the single-domain orthorhombic AF

phase of iron pnictides [48–50,54–56]. To see this, Fig. 4(n) compares the temperature dependence of the band splittings in pressure-free and uniaxial pressure-strained NaFeAs single crystals [50]. Without applied uniaxial pressure, the band splitting of an unstrained (twinned) NaFeAs crystal begins at T_s. For a detwinned crystal in the presence of uniaxial strain, the band splitting due to orbital anisotropy is resolvable up to at least 70 K, well above T_s [50] [Fig. 4(n)]. The comparison with and without strain shows that this elevation of band splitting to higher temperatures is a direct result of uniaxial strain, which acts like a biasing field to the nematic order just like a magnetic field does to a ferromagnetic order. It is likely that a small anisotropy persists as long as the biasing field—strain in this case—is present, but unresolvable due to finite energy resolution in the ARPES experiments. This is consistent with the observation that while low-energy spin excitations in BaFe$_2$As$_2$ ($T_N \approx T_s \approx 140$ K) have a small anisotropy at all temperatures below 250 K, the enhancement of spin excitation anisotropy below T^* ($T_N, T_s < T^* \ll 250$ K) is associated
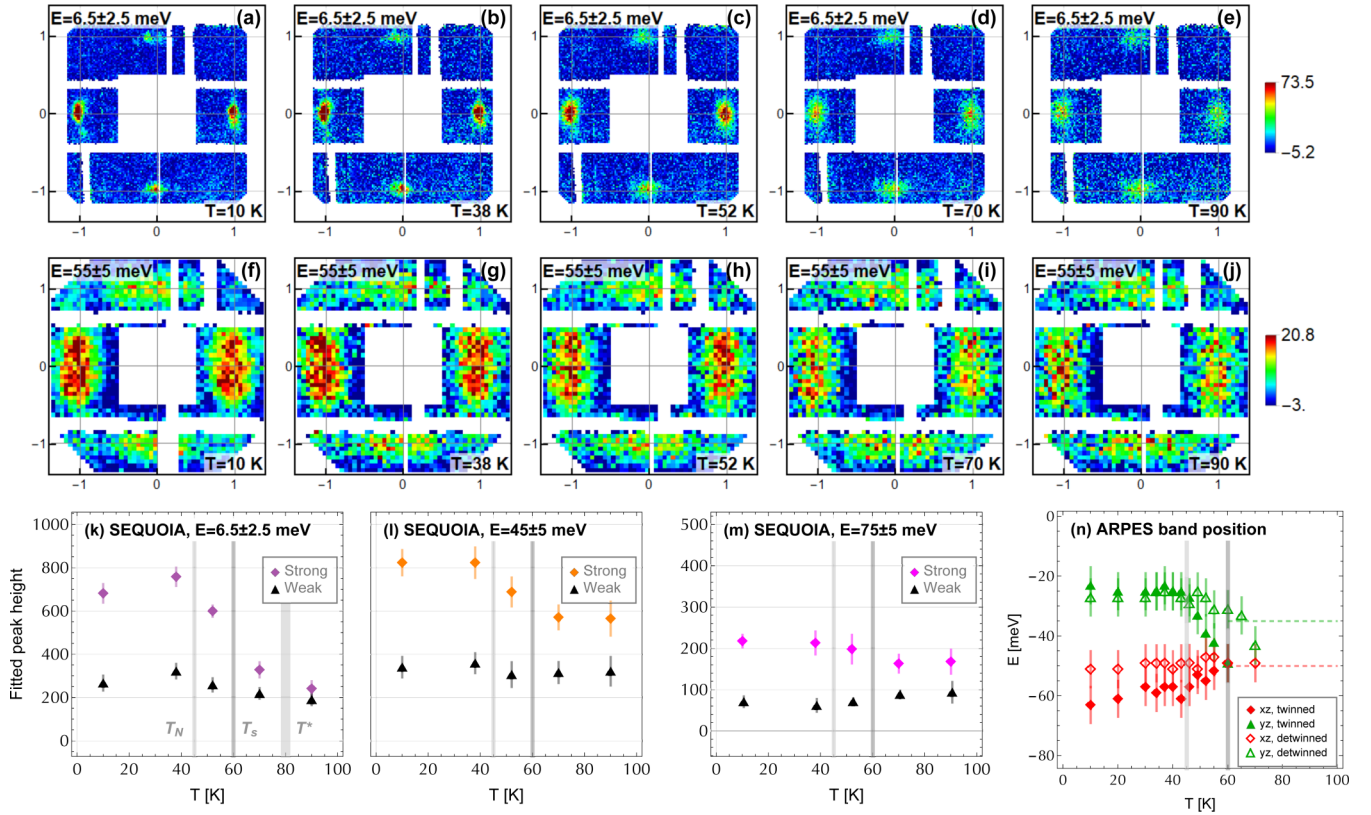
FIG. 4. (a)–(e) Inelastic neutron scattering data from SEQUOIA at constant energy transfer $E = 6.5 \pm 2.5$ meV, at temperatures $T = 10$, 38, 52, 70, and 90 K, after background subtraction [42] and with constant color scale shown at right. (f)–(j) The same as (a)–(e) at energy transfer $E = 55 \pm 5$ meV. (k), (l) Peak height of Gaussian fits to transverse cuts, at (k) $E = 6.5 \pm 2.5$ meV and (l) 45 ± 5 meV, in absolute units. (m) Peak height of the incommensurate (d_{yz}) peak, fitted along transverse cuts at $E = 75 \pm 5$ meV to a two-peak model including one peak constrained to the position $\mathbf{Q} = (1, 1)$ as described in the Supplementary Material [42]. (n) Temperature dependence of the d_{yz} (green) and d_{xz} (red) band positions measured on twinned and detwinned crystals of NaFeAs from Ref. [50]. The light and dark shaded vertical lines in (k)–(n) mark zero pressure T_N and T_s, respectively. The wide shaded line in (k) indicates T^*.

with resistivity anisotropy and band splitting [56]. Although the exact uniaxial pressures used in Ref. [50] and Figs. 4(k)–4(m) are unknown, it is clear that the T^* associated with the enhanced spin excitation anisotropy occurs at approximately the band-splitting temperature of strained NaFeAs.

To test the temperature dependence of the spin excitation anisotropy for energies above $E = 80$ meV, we show in Figs. 5(a)–5(e) 2D raw images of the $E = 100 \pm 10$ meV spin excitations at $T = 10$, 38, 52, 70, 90 K, respectively, obtained on SEQUOIA with $E_i = 150$ meV. On warming across T_N and T_s, spin excitations have approximate C_4 rotational symmetry with weak anisotropy, but are essentially temperature independent. Figure 5(f) shows the 2D raw image of spin excitations at $E = 140 \pm 10$ meV obtained on SEQUOIA with $E_i = 250$ meV and $T = 10$ K, again revealing approximate C_4 rotational symmetry with weak anisotropy. Comparing these results with the combined DFT+DMFT calculations at $E = 140$ meV for d_{xz}-d_{xz} [Fig. 5(g)], d_{yz}-d_{yz} [Fig. 5(h)], and d_{xy}-d_{xy} [Fig. 5(i)] intraorbital scattering channels, we see that spin excitations with energies above $E = 100$ meV are peaked at the $(\pm 1, \pm 1)$ positions, which is most consistent with the d_{xy}-d_{xy} intraorbital scattering [Fig. 5(i)].

To understand the small, weakly temperature dependent, spin excitation anisotropy observed at all energies in Figs. 4 and 5, we note that the applied uniaxial pressure necessary

to detwin the sample also induces an orthorhombic lattice distortion and a strain field at all temperatures [57]. For an applied pressure of $P \approx 20$ MPa, the pressure-induced lattice parameter distortion in $BaFe_2As_2$ at temperatures well above the zero-pressure T_s is weakly temperature dependent and about 15% of the intrinsic orthorhombic lattice distortion below T_s (see Fig. 1(c) of Ref. [57]). Since the resistivity and spin excitation anisotropy at temperatures above the zero-pressure T_s increase with increasing uniaxial pressure [54–56], it is safe to assume that the uniaxial pressure-induced strain field in NaFeAs will produce a small C_4 rotational symmetry breaking spin excitation component at all energies and temperatures.

IV. DFT+DMFT CALCULATIONS AND COMPARISON WITH DATA

DFT+DMFT [58] was employed to compute the electronic structure and spin dynamics of NaFeAs and $BaFe_2As_2$ in the nematic state. The full-potential linearized augmented plane wave method implemented in WIEN2k [59] was used for the density functional theory part in conjunction with the Perdew-Burke-Ernzerhof generalized gradient approximation [60] of the exchange correlation functional. DFT+DMFT was implemented on top of WIEN2k and documented in Ref. [61].
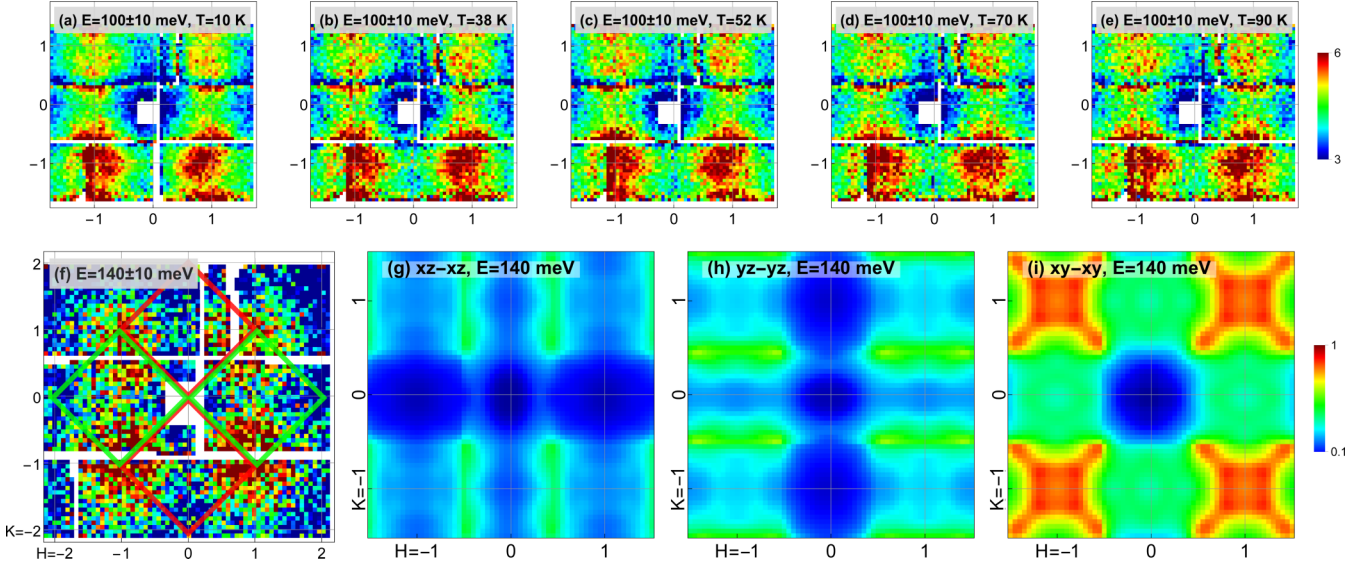
FIG. 5. (a)–(e) 2D images of spin excitation raw data of $E = 100 \pm 10$ meV obtained on SEQUOIA with $E_i = 150$ meV along the c axis at temperatures $T = 10, 38, 52, 70,$ and 90 K. The streaks in the images represent the positions of detector gaps which are slightly $\mathbf{Q}$-dependent in the $E = 90$–110 meV energy window at $E_i = 150$ meV, thus leading to a smearing effect. (f) 2D image of spin wave raw data of $E = 140 \pm 10$ meV at 10 K obtained on SEQUOIA with $E_i = 250$ meV along the c axis. The green and red boxes are intensity integration regions for the strong and weak positions, respectively. The DFT+DMFT calculation for $E = 140 \pm 10$ meV in the d_{xz}-d_{xz} (g), d_{yz}-d_{yz} (h), and d_{xy}-d_{xy} (i) intraorbital scattering channels.

In the DFT+DMFT calculations, the electronic charge was computed self-consistently on DFT+DMFT density matrix. The quantum impurity problem was solved by the continuous time quantum Monte Carlo method [62,63] with a Hubbard $U = 5.0$ eV and Hund's rule coupling $J_H = 0.8$ eV in the paramagnetic state [9,34]. Such a choice of the Hund's rule coupling is essential for the large spin excitation strength and small spin wave bandwidth. If the Hund's rule coupling is small, there will be very small local spin moment, very weak spin excitations, and large spin wave bandwidth. There are also hybridizations of the d_{xz}, d_{yz}, and d_{xy} orbitals between the neighboring Fe atoms, and therefore affecting the interorbital contributions of the total spin excitations. Since the strength of the interorbital contribution lies between the individual intraorbital contributions, we can focus on the intraorbital contribution to obtain a simplified but largely accurate picture.

The Bethe-Salpeter equation is used to compute the dynamic spin susceptibility where the bare susceptibility is computed using the converged DFT+DMFT Green's function while the two-particle vertex is directly sampled using the continuous-time quantum Monte Carlo method after achieving full self-consistency of the DFT+DMFT density matrix. We assume that the two-particle vertex Γ is the same in the nematic state as in the paramagnetic state. The detailed method of computing the dynamic spin susceptibility is documented in Ref. [34] and was shown to be able to compute accurately the spin dynamics of many iron pnictide superconductors. To simulate the nematic state, 50 meV and 80 meV on-site energy splitting of the d_{xz} and d_{yz} orbitals were added to the DFT+DMFT converged solutions of the paramagnetic state for NaFeAs and BaFe$_2$As$_2$, respectively, consistent with ARPES measurements at the (1,0) and (0,1) electron pockets [49,50]. The experimental crystal structures of NaFeAs [64] and BaFe$_2$As$_2$ [65] were used in the calculations.

Figures 6(a), 6(c) and 6(e) show the calculated spin wave dispersions of NaFeAs from the d_{xz}, d_{yz}, and d_{xy} orbital channels, respectively. Figures 6(b), 6(d) and 6(f) show similar calculations for BaFe$_2$As$_2$. The data points overlaid in Figs. 6(c) and 6(d) are the spin wave dispersion relations of NaFeAs and BaFe$_2$As$_2$, respectively, determined from neutron scattering experiments [35]. By comparing Fig. 6 with Fig. 3 for NaFeAs and those of detwinned BaFe$_2$As$_2$ [35], we conclude that spin waves below $E_{\mathrm{crossover}} \approx 100$ meV along the $\mathbf{Q}_{\mathrm{strong}}$ direction arise predominantly from the d_{yz} channel. For $E \gtrsim 110$ meV, the neutron data show the most spectral weight at the $\mathbf{Q}_{xy} = (1, 1)$ position [Fig. 3(f)], consistent with the calculations in the d_{xy} channel but not the d_{yz} channel. This is also the case for spin excitations at $E = 140 \pm 10$ meV [Fig. 5(f)]. The spin excitations centered at $\mathbf{Q}_{xy} = (1, 1)$ remain partially anisotropic at least as high as 150 meV, probably arising from the applied pressure-induced lattice anisotropy. There is also experimental [49,66] and theoretical [67] evidence that the d_{xy}-dominated bands may participate in the broken C_4 rotational symmetry.

To quantitatively compare the observed spin wave anisotropy in NaFeAs with DFT+DMFT calculations, we show the local dynamic susceptibility $\chi''(E)$ in Fig. 7(a) as a function of energy, integrated over the green [$\mathbf{Q}_{\mathrm{strong}} = (\pm1, 0)$] and red [$\mathbf{Q}_{\mathrm{weak}} = (0, \pm1)$] diamond-shaped zones shown in Fig. 1(e). Each diamond has the area of one magnetic unit cell. The intensity in each region is converted into absolute units of magnetic susceptibility by fitting and subtracting the background and correcting for the magnetic form factor of Fe^{2+} and the Bose factor, as described in the Supplemental Material [42]. The resulting integrated intensity from the strong and weak positions can be averaged to roughly match previously published data [30,68]. The green, red, and blue dashed lines represent the DFT+DMFT results from the d_{yz},
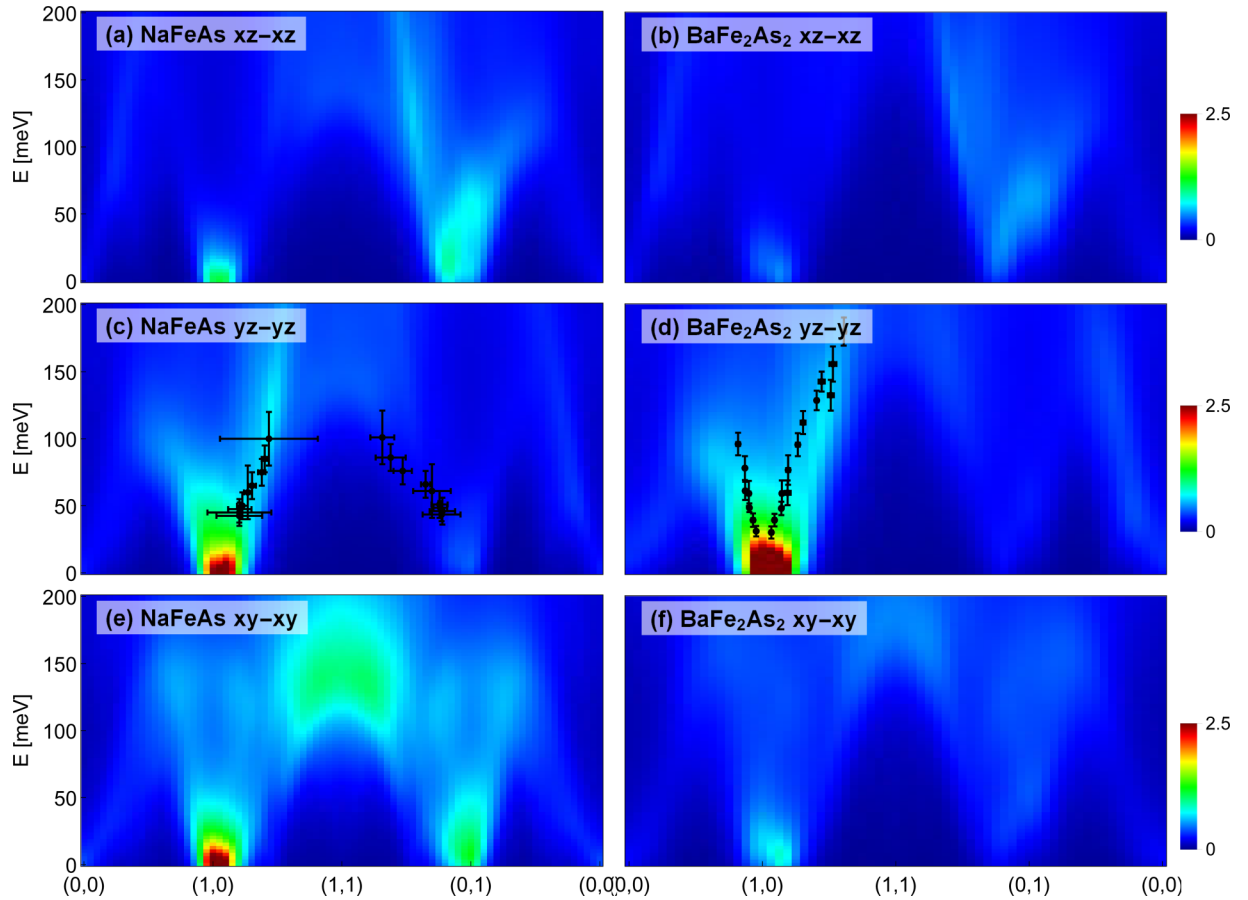
FIG. 6. DFT+DMFT intensity along **Q**-E cuts around the high-symmetry paths in the in-plane orthorhombic unit cell, for NaFeAs [(a), (c), (e)] and BaFe$_2$As$_2$ [(b), (d), (f)], in (a), (b) the d_{xz}-d_{xz}, (c), (d) d_{yz}-d_{yz}, and (e), (f) d_{xy}-d_{xy} intraorbital scattering channels. The peak positions from neutron scattering data closely match the DFT+DMFT intensity in the d_{yz}-d_{yz} channel for both (c) NaFeAs and (d) BaFe$_2$As$_2$, with data taken from [35]. Above $\sim$110 meV, spin fluctuations are observed at (1,1) and are consistent with the d_{xy}-d_{xy} scattering channel as shown in the constant-energy slices in Fig. 3. Spin fluctuations at (1,1) are pushed above $E \approx 150$ meV in BaFe$_2$As$_2$ and persist to the band top of nearly 300 meV, showing that the larger overall bandwidth of BaFe$_2$As$_2$ is controlled by d_{xy}-d_{xy} fluctuations.

d_{xz}, and d_{xy} intraorbital scattering. Experimental results from SEQUOIA and MERLIN are clearly marked.

Figure 6(b) shows the spin wave energy dependent anisotropy, defined as $\delta = (I_s - I_w)/(I_s + I_w)$ [69], and its comparison with δ from the DFT+DMFT calculation for different orbitals. While the observed spin wave anisotropies are similar for energies below $E \approx 80$ meV for SEQUOIA and MERLIN measurements, they are slightly different at higher energies, due in part to different applied uniaxial pressures in these two experiments. The spin wave anisotropy decreases with increasing energy, and changes from the C_2 to C_4 rotational symmetry around $E_{crossover} \approx 100$ meV (Figs. 3–5). While the low-energy spin excitations change anisotropy at temperatures slightly above T_s, spin excitations at energies above $E_{crossover}$ have approximate C_4 rotational symmetry that does not change across T_s (Figs. 4, 5). These results clearly reveal orbital selective spin waves, suggesting that low-energy spin waves are mostly controlled by the d_{yz} orbital scattering associated with the nematic order below T_s, while high-energy spin waves near the zone boundary are determined by the electronic bandwidth of the d_{xy} orbitals [8]. The electronic nematic phase below T_s is associated with the splitting of the d_{yz} and d_{xz} orbital bands and spin wave anisotropy between

$\mathbf{Q}_{strong}$ and $\mathbf{Q}_{weak}$ [49,50], although such an effect is already present above T_s due to applied uniaxial pressure (Fig. 4) [8,55]. In the paramagnetic state at a temperature well above T_s, spin wave anisotropy between $\mathbf{Q}_{strong}$ and $\mathbf{Q}_{weak}$ becomes weakly temperature dependent together with the vanishing splitting of the d_{yz} and d_{xz} orbital bands [8,55]. Therefore, the energy splitting of the d_{yz} and d_{xz} orbital bands is directly associated with the electronic and spin nematic phase, and spin waves in NaFeAs are orbital selective and controlled by the electronic properties of the system.

The observation of low-energy d_{yz}-d_{yz} fluctuations is consistent with the idea that these excitations are itinerant and responsible for superconducting pairing [21–23], while the d_{xy}-d_{xy} fluctuations are more localized and do not observably change across the electron-doped superconducting dome [68]. Since the spin fluctuation spectrum in BaFe$_2$As$_2$ also exhibits qualitatively similar results to that in NaFeAs, and with DFT+DMFT calculations showing high-energy scattering centered at $\mathbf{Q}_{xy} = (1, 1)$ but extending to higher energy in BaFe$_2$As$_2$, we conclude that the overall magnetic bandwidth in iron pnictides is controlled by localized magnetic superexchange interactions. With increased pnictogen height above the iron plane and resulting increased electron correlations on
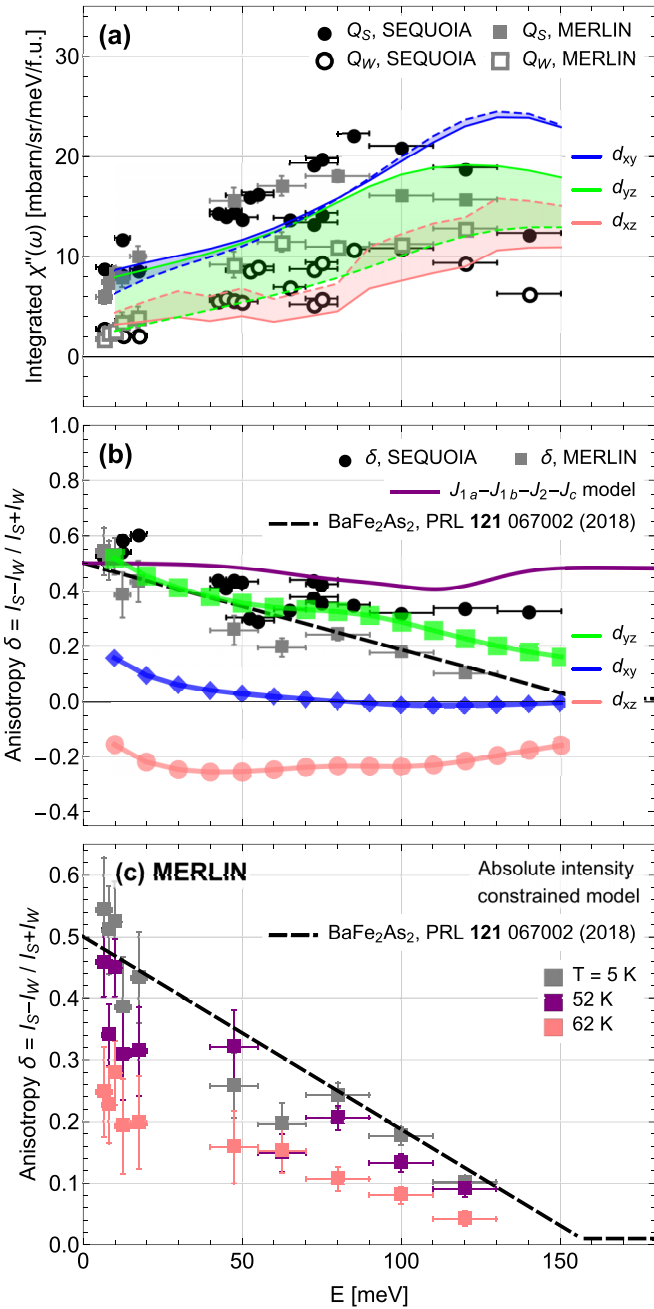
FIG. 7. (a) Energy dependence of the momentum-integrated local dynamic magnetic susceptibility, from inelastic neutron scattering, for the strong (solid symbols) and weak positions (open symbols) at 10 K. Orbital selective DFT+DMFT calculation, with the strong-side integrated intensity shown as solid lines and weak-side intensity as dashed lines, demonstrates that d_{yz}-d_{yz} fluctuations (green) can explain the observed anisotropy. (b) Anisotropy of the integrated intensity, demonstrating excellent agreement between experimental observations and d_{yz}-d_{yz} intraorbital component of χ'' computed by DFT+DMFT up to at least 100 meV. The purple line shows the results of linear spin wave theory using the Heisenberg parameters in [30]. (c) Anisotropy of spin excitations at 5 K ($\ll T_N$), 52 K ($> T_N$ and $< T_s$), and 62 K (larger than zero pressure T_s). The dashed black lines in (b), (c) are the results obtained for BaFe$_2$As$_2$ reported in [35].

moving from BaFe$_2$As$_2$ to NaFeAs, we see a clear reduction in energy for spin excitations at the $\mathbf{Q}_{xy} = (1, 1)$ position, suggesting that spin excitations around the $\mathbf{Q}_{xy} = (1, 1)$ position are mostly associated with the d_{xy} orbital [11,48–50]. These results are consistent with the notion that increased electron correlations in NaFeAs are accompanied by reduced electronic bandwidth in the d_{xy} orbital [8] and spin wave energy bandwidth (and the magnetic exchange coupling J) [30].

Our conclusion that the microscopic origin of magnetic scattering is orbitally selective is not in contradiction with other models previously used for the iron pnictides. Although spin excitations in detwinned NaFeAs can be much better understood by orbital selective scattering processes, one should also be able to parametrize these excitations with a Heisenberg Hamiltonian which has no information concerning the orbital nature of the excitations [30]. Since superconductivity in iron pnictides arises from electron/hole-doped antiferromagnets, one can use the t-J model to estimate high-temperature superconductivity states regardless of the microscopic origin of spin excitations [70]. In the notion of spin fluctuation driven superconductivity [1], the superconducting condensation energy of the system should be dominated by the change in magnetic exchange energy between the normal (N) and superconducting (S) phase at zero temperature $\Delta E_{ex}(T = 0)$. Within the t-J model, this means that $\Delta E_{ex}(T) = 2J[\langle \mathbf{S}_{i+x} \cdot \mathbf{S}_i \rangle_N - \langle \mathbf{S}_{i+x} \cdot \mathbf{S}_i \rangle_S]$, where J is the nearest-neighbor magnetic exchange coupling and $\langle \mathbf{S}_{i+x} \cdot \mathbf{S}_i \rangle$ is the magnetic scattering in absolute units at temperature T [71]. In this picture, the quasiparticle excitations across the nested hole-electron Fermi surfaces in the nematic phase arise mostly from the d_{yz}-d_{yz} intraorbital excitations, and give rise to the C_2 neutron spin resonance seen in different families of iron-based superconductors [21–23]. The increased electron-electron correlations from BaFe$_2$As$_2$ to NaFeAs, reflected in reduced bandwidth of the d_{xy} orbital and high-energy spin excitations [30], correspond to the reduced magnetic exchange coupling J. Therefore, localized electrons in the d_{xy} orbital and associated high-energy spin excitations with C_4 symmetry are also important for superconductivity of iron-based materials.

V. CONCLUSIONS

In summary, we have used inelastic neutron scattering to study spin waves of detwinned crystals of NaFeAs. By comparing the energy and temperature dependence of the spin wave anisotropy with DFT+DMFT calculations, we conclude that spin waves in iron pnictides are orbital selective. While the d_{xy} orbital scattering processes control the bandwidth of spin fluctuations in the iron pnictides, the low-energy spin fluctuations may arise through Fermi surface nesting of itinerant electrons with d_{yz} orbital character below T_s, and coupled to the nematic phase transition. Superconductivity in nematic-ordered iron pnictides may therefore be controlled by Fermi surface nesting of itinerant electrons with d_{yz} orbital character while high-energy spin excitations asso-

ciated with the d_{xy} orbital and electron correlations are also important.

[1] D. J. Scalapino, Rev. Mod. Phys. **84**, 1383 (2012).

[2] P. C. Dai, Rev. Mod. Phys. **87**, 855 (2015).

[3] P. A. Lee, N. Nagaosa, and X. G. Wen, Rev. Mod. Phys. **78**, 17 (2006).

[4] D. J. Scalapino, Phys. Rep. **250**, 329 (1995).

[5] G. R. Stewart, Rev. Mod. Phys. **83**, 1589 (2011).

[6] P. J. Hirschfeld, M. M. Korshunov, and I. I. Mazin, Rep. Prog. Phys. **74**, 124508 (2011).

[7] Q. Si, R. Yu, and E. Abrahams, Nat. Rev. Mater. **1**, 16017 (2016).

[8] M. Yi, Y. Zhang, Z.-X. Shen, and D. Lu, npj Quantum Mater. **2**, 57 (2017).

[9] Z. P. Yin, K. Haule, and G. Kotliar, Nat. Mater. **10**, 932 (2011).

[10] R. M. Fernandes, A. V. Chubukov, and J. Schmalian, Nat. Phys. **10**, 97 (2014).

[11] M. D. Watson, T. K. Kim, L. C. Rhodes, M. Eschrig, M. Hoesch, A. A. Haghighirad, and A. I. Coldea, Phys. Rev. B **94**, 201107(R) (2016).

[12] L. Fanfarillo, J. Mansart, P. Toulemonde, H. Cercellier, P. Le Fèvre, F. Bertran, B. Valenzuela, L. Benfatto, and V. Brouet, Phys. Rev. B **94**, 155138 (2016).

[13] F.-C. Hsu, J.-Y. Luo, K.-W. Yeh, T.-K. Chen, T.-W. Huang, P. M. Wu, Y.-C. Lee, Y.-L. Huang, Y.-Y. Chu, D.-C. Yan, and M.-K. Wu, Proc. Natl Acad. Sci. USA **105**, 14262 (2008).

[14] T. M. McQueen, A. J. Williams, P. W. Stephens, J. Tao, Y. Zhu, V. Ksenofontov, F. Casper, C. Felser, and R. J. Cava, Phys. Rev. Lett. **103**, 057002 (2009).

[15] A. E. Böhmer and A. Kreisel, J. Phys.: Condens. Matter **30**, 023001 (2018).

[16] M. Yi, Z.-K. Liu, Y. Zhang, R. Yu, J.-X. Zhu, J. J. Lee, R. G. Moore, F. T. Schmitt, W. Li, S. C. Riggs, J.-H. Chu, B. Lv, J. Hu, M. Hashimoto, S.-K. Mo, Z. Hussain, Z. Q. Mao, C. W. Chu, I. R. Fisher, Q. Si, Z.-X. Shen, and D. H. Lu, Nat. Commun. **6**, 7777 (2015).

[17] H. Miao, Z. P. Yin, S. F. Wu, J. M. Li, J. Ma, B.-Q. Lv, X. P. Wang, T. Qian, P. Richard, L.-Y. Xing, X.-C. Wang, C. Q. Jin, K. Haule, G. Kotliar, and H. Ding, Phys. Rev. B **94**, 201109(R) (2016).

[18] Z. P. Yin, K. Haule, and G. Kotliar, Phys. Rev. B **86**, 195141 (2012).

[19] P. O. Sprau, A. Kostin, A. Kreisel, A. E. Böhmer, V. Taufour, P. C. Canfield, S. Mukherjee, P. J. Hirschfeld, B. M. Andersen, and J. C. Séamus Davis, Science **357**, 75 (2017).

[20] A. V. Chubukov, M. Khodas, and R. M. Fernandes, Phys. Rev. X **6**, 041045 (2016).

[21] T. Chen, Y. Chen, A. Kreisel, X. Lu, A. Schneidewind, Y. Qiu, J. T. Park, T. G. Perring, J. R. Stewart, H. Cao, R. Zhang, Y. Li, Y. Rong, Y. Wei, B. M. Andersen, P. J. Hirschfeld, C. Broholm, and P. Dai, Nat. Mater. **18**, 709 (2019).

[22] W. Wang, J. T. Park, R. Yu, Y. Li, Y. Song, Z. Zhang, A. Ivanov, J. Kulda, and P. Dai, Phys. Rev. B **95**, 094519 (2017).

[23] L. Tian, P. Liu, Z. Xu, Y. Li, Z. Lu, H. C. Walker, U. Stuhr, G. Tan, X. Lu, and P. Dai, Phys. Rev. B **100**, 134509 (2019).

[24] M. Eschrig, Adv. Phys. **55**, 47 (2006).

[25] T. A. Maier and D. J. Scalapino, Phys. Rev. B **78**, 020514(R) (2008).

[26] R. Zhang, W. Wang, T. A. Maier, M. Wang, M. B. Stone, S. Chi, B. Winn, and P. Dai, Phys. Rev. B **98**, 060502(R) (2018).

[27] D. S. Inosov, J. T. Park, P. Bourges, D. L. Sun, Y. Sidis, A. Schneidewind, K. Hradil, D. Haug, C. T. Lin, B. Keimer, and V. Hinkov, Nat. Phys. **6**, 178 (2010).

[28] C. H. Lee, P. Steffens, N. Qureshi, M. Nakajima, K. Kihou, A. Iyo, H. Eisaki, and M. Braden, Phys. Rev. Lett. **111**, 167002 (2013).

[29] F. Waßer, J. T. Park, S. Aswartham, S. Wurmehl, Y. Sidis, P. Steffens, K. Schmalzl, B. Büchner, and M. Braden, npj Quantum Mater. **4**, 59 (2019).

[30] C. Zhang, L. W. Harriger, Z. Yin, W. Lv, M. Wang, G. Tan, Y. Song, D. L. Abernathy, W. Tian, T. Egami, K. Haule, G. Kotliar, and P. Dai, Phys. Rev. Lett. **112**, 217202 (2014).

[31] J. Zhao, D. T. Adroja, D.-X. Yao, R. Bewley, S. Li, X. F. Wang, G. Wu, X. H. Chen, J. Hu, and P. C. Dai, Nat. Phys. **5**, 555 (2009).

[32] L. W. Harriger, H. Q. Luo, M. S. Liu, C. Frost, J. P. Hu, M. R. Norman, and Pengcheng Dai, Phys. Rev. B **84**, 054544 (2011).

[33] R. A. Ewings, T. G. Perring, J. Gillett, S. D. Das, S. E. Sebastian, A. E. Taylor, T. Guidi, and A. T. Boothroyd, Phys. Rev. B **83**, 214519 (2011).

[34] Z. P. Yin, K. Haule, and G. Kotliar, Nat. Phys. **10**, 845 (2014).

[35] X. Lu, D. D. Scherer, D. W. Tam, W. Zhang, R. Zhang, H. Luo, L. W. Harriger, H. C. Walker, D. T. Adroja, B. M. Andersen, and P. Dai, Phys. Rev. Lett. **121**, 067002 (2018).

[36] Q. Huang, Y. Qiu, Wei Bao, M. A. Green, J. W. Lynn, Y. C. Gasparovic, T. Wu, G. Wu, and X. H. Chen, Phys. Rev. Lett. **101**, 257003 (2008).

[37] M. G. Kim, R. M. Fernandes, A. Kreyssig, J. W. Kim, A. Thaler, S. L. Bud'ko, P. C. Canfield, R. J. McQueeney, J. Schmalian, and A. I. Goldman, Phys. Rev. B **83**, 134522 (2011).

[38] S. Li, C. de la Cruz, Q. Huang, G. F. Chen, T.-L. Xia, J. L. Luo, N. L. Wang, and P. Dai, Phys. Rev. B **80**, 020504(R) (2009).

[39] G. Tan, Y. Song, C. Zhang, L. Lin, Z. Xu, T. Hou, W. Tian, H. Cao, S. Li, S. Feng, and P. Dai, Phys. Rev. B **94**, 014509 (2016).

[40] G. E. Granroth, A. I. Kolesnikov, T. E. Sherline, J. P. Clancy, K. A. Ross, J. P. C. Ruff, B. D. Gaulin, and S. E. Nagler, J. Phys.: Conf. Ser. **251**, 12058 (2010).

[41] R. I. Bewley, T. Guidi, and S. Bennington, Notiziario Neutroni e Luce di Sincrotrone **14**, 22 (2009).

[42] See Supplemental Material at http://link.aps.org/supplemental/10.1103/PhysRevB.102.054430 for additional data and analysis, which include Refs. [72,73].

[43] C. Dhital, Z. Yamani, W. Tian, J. Zeretsky, A. S. Sefat, Z. Wang, R. J. Birgeneau, and S. D. Wilson, Phys. Rev. Lett. **108**, 087001 (2012).

[44] C. Dhital, T. Hogan, Z. Yamani, R. J. Birgeneau, W. Tian, M. Matsuda, A. S. Sefat, Z. Wang, and S. D. Wilson, Phys. Rev. B **89**, 214404 (2014).

[45] Y. Song, S. V. Carr, X. Y. Lu, C. L. Zhang, Z. C. Sims, N. F. Luttrell, S. X. Chi, Y. Zhao, J. W. Lynn, and P. C. Dai, Phys. Rev. B **87**, 184511 (2013).

[46] David W. Tam, Yu Song, Haoran Man, Sky C. Cheung, Zhiping Yin, Xingye Lu, Weiyi Wang, Benjamin A. Frandsen, Lian Liu, Zizhou Gong, Takashi U. Ito, Yipeng Cai, Murray N. Wilson, Shengli Guo, Keisuke Koshiishi, Wei Tian, Bassam Hitti, Alexandre Ivanov, Yang Zhao, Jeffrey W. Lynn, Graeme M. Luke, Tom Berlijn, Thomas A. Maier, Yasutomo J. Uemura, and Pengcheng Dai, Phys. Rev. B **95**, 060505(R) (2017).

[47] X. Lu, J. T. Park, R. Zhang, H. Luo, A. H. Nevidomskyy, Q. Si, and P. C. Dai, Science **345**, 657 (2014).

[48] Y. Zhang, M. Yi, Z.-K. Liu, W. Li, J. J. Lee, R. G. Moore, M. Hashimoto, M. Nakajima, H. Eisaki, S.-K. Mo, Z. Hussain, T. P. Devereaux, Z.-X. Shen, and D. H. Lu, Phys. Rev. B **94**, 115153 (2016).

[49] Y. Zhang, C. He, Z. R. Ye, J. Jiang, F. Chen, M. Xu, Q. Q. Ge, B. P. Xie, J. Wei, M. Aeschlimann, X. Y. Cui, M. Shi, J. P. Hu, and D. L. Feng, Phys. Rev. B **85**, 085121 (2012).

[50] M. Yi, D. H. Lu, R. G. Moore, K. Kihou, C.-H. Lee, A. Iyo, H. Eisaki, T. Yoshida, A. Fujimori, and Z.-X. Shen, New J. Phys. **14**, 073019 (2012).

[51] J. Zhang, R. Sknepnek, and J. Schmalian, Phys. Rev. B **82**, 134527 (2010).

[52] M. D. Johannes, I. I. Mazin, and C. A. Howells, Phys. Rev. B **73**, 205102 (2006).

[53] Y. Li, Z. Yamani, Y. Song, W. Wang, C. Zhang, D. W. Tam, T. Chen, D. Hu, Z. Xu, S. Chi, K. Xia, L. Zhang, S. Cui, W. Guo, Z. Fang, Y. Liu, and P. Dai, Phys. Rev. X **8**, 021056 (2018).

[54] J.-H. Chu, J. G. Analytis, K. De Greve, P. L. McMahon, Z. Islam, Y. Yamamoto, and I. R. Fisher, Science **329**, 824 (2010).

[55] H. R. Man, R. Zhang, J. T. Park, Xingye Lu, J. Kulda, A. Ivanov, and P. C. Dai, Phys. Rev. B **97**, 060507(R) (2018).

[56] D. W. Tam, W. Y. Wang, L. Zhang, Y. Song, R. Zhang, S. V. Carr, H. C. Walker, T. G. Perring, D. T. Adroja, and P. C. Dai, Phys. Rev. B **99**, 134519 (2019).

[57] X. Y. Lu, K.-F. Tseng, T. Keller, W. L. Zhang, D. Hu, Y. Song, H. R. Man, J. T. Park, H. Q. Luo, S. L. Li, A. H. Nevidomskyy, and P. C. Dai, Phys. Rev. B **93**, 134519 (2016).

[58] G. Kotliar, S. Y. Savrasov, K. Haule, V. S. Oudovenko, O. Parcollet, and C. A. Marianetti, Rev. Mod. Phys. **78**, 865 (2006).

[59] P. Blaha, K. Schwarz, G. Madsen, D. Kvasnicka, and J. Luitz, *WIEN2k, An Augmented Plane Wave+Local Orbitals Program for Calculating Crystal Properties* (Karlheinz Schwarz, Technische Universität Wien, Austria, 2001).

[60] J. P. Perdew, K. Burke, and M. Ernzerhof, Phys. Rev. Lett. **77**, 3865 (1996).

[61] K. Haule, C.-H. Yee, and K. Kim, Phys. Rev. B **81**, 195107 (2010).

[62] K. Haule, Phys. Rev. B **75**, 155113 (2007).

[63] P. Werner, A. Comanac, L. de' Medici, M. Troyer, and A. J. Millis, Phys. Rev. Lett. **97**, 076405 (2006).

[64] D. R. Parker, M. J. Pitcher, P. J. Baker, I. Franke, T. Lancaster, S. J. Blundell, and S. J. Clarke, Chem. Commun. (2009) 2189.

[65] M. Rotter, M. Tegel, D. Johrendt, I. Schellenberg, W. Hermes, and R. Pöttgen, Phys. Rev. B **78**, 020503(R) (2008).

[66] M. Yi, H. Pfau, Y. Zhang, Y. He, H. Wu, T. Chen, Z. R. Ye, M. Hashimoto, R. Yu, Q. Si, D.-H. Lee, Pengcheng Dai, Z.-X. Shen, D. H. Lu, and R. J. Birgeneau, Phys. Rev. X **9**, 041049 (2019).

[67] M. H. Christensen, J. Kang, B. M. Andersen, and R. M. Fernandes, Phys. Rev. B **93**, 085136 (2016).

[68] S. V. Carr, C. Zhang, Y. Song, G. Tan, Y. Li, D. L. Abernathy, M. B. Stone, G. E. Granroth, T. G. Perring, and P. Dai, Phys. Rev. B **93**, 214506 (2016).

[69] Y. Song, X. Lu, D. L. Abernathy, D. W. Tam, J. L. Niedziela, W. Tian, H. Luo, Q. Si, and P. Dai, Phys. Rev. B **92**, 180504(R) (2015).

[70] N. Karchev, Phys. Rev. B **57**, 10913 (1998).

[71] M. Wang, C. Zhang, X. Lu, G. T. Tan, H. Luo, Y. Song, M. Y. Wang, X. Zhang, E. A. Goremychkin, T. G. Perring, T. A. Maier, Z. P. Yin, K. Haule, G. Kotliar, and P. Dai, Nat. Commun. **4**, 2874 (2013).

[72] D. W. Tam, H.-H. Lai, J. Hu, X. Lu, H. C. Walker, D. L. Abernathy, J. L. Niedziela, T. Weber, M. Enderle, Y. Su, Z. Q. Mao, Q. Si, and P. Dai, Phys. Rev. B **100**, 054405 (2019).

[73] Q. Wang, Y. Shen, B. Pan, X. Zhang, K. Ikeuchi, K. Iida, A. D. Christianson, H. C. Walker, D. T. Adroja, M. Abdel-Hafiez, X. Chen, D. A. Chareev, A. N. Vasiliev, and J. Zhao, Nat. Commun. **7**, 12182 (2016).